ACS Sustainable Chemistry & Engineering

pubs.acs.org/journal/ascecg

Research Article

Selective Formation of the $Li_4Mn_5O_{12}$ Surface Spinel Phase in Sulfur-Doped Li-Excess-Layered Cathode Materials for Improved Cycle Life

Yongju Lee, Tae-Hee Kim, Young-Kyun Kwon,* Jaewook Shin,* and EunAe Cho*

Cite This: *ACS Sustainable Chem. Eng.* 2020, 8, 8037−8048

Read Online

ACCESS | Metrics & More | Article Recommendations | Supporting Information

ABSTRACT: The Li-excess-layered cathode (LLC) as a lithium-ion battery (LIB) cathode has received significant attention due to the need for high specific energy density. However, these cathode materials are associated with unwanted surface structural transformations from the layered to the spinel phase. This transformation hinders Li^+ ion transport by lattice mismatching and Jahn−Teller distortion. Furthermore, it causes Mn ion dissolution, leading to the formation of an insulating rock-salt phase on the surface. This can deteriorate the electrochemical cycle retention and rate capability, limiting their use in practical applications. In order to address these issues, we dope S into the surface of the LLC material (S-LLC), $Li_{1.2}Mn_{0.54}Ni0._{13}Co_{0.13}O_{2-x}S_x$, to tailor the surface transformation and thus electrochemical performance outcomes. This type of sulfurization strategy can induce the formation of the $Li_4Mn_5O_{12}$ spinel phase, which can relieve the structural incompatibility and Mn dissolution. The S-LLC shows excellent electrochemical performance; the S-LLC has a first specific discharge capacity of 233.7 mAh/g and a cycle retention of 95.5% after 200 cycles with good rate capability. This work provides an insight into a novel anion doping method for the selective formation of a desirable surface spinel phase for high energy-density cathode materials for LIBs.

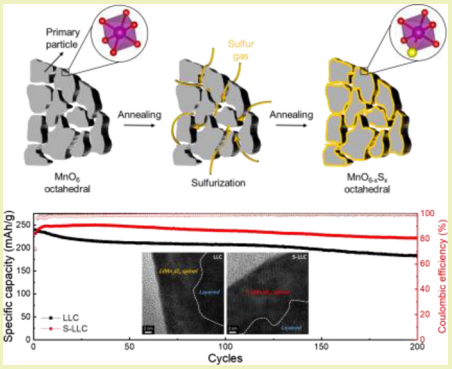

KEYWORDS: *lithium-ion batteries, Li-excess cathode, anion doping, surface spinel, DFT calculation*

INTRODUCTION

Lithium-ion batteries (LIBs) are the promising energy sources for mobile electronics, electric vehicles (EVs), and energy storage systems (ESSs).[1,2] However, current LIBs cannot meet the demanding energy requirements given that the cathode materials, such as $LiCoO_2$,[3,4] $LiFePO_4$,[5−7] $LiMn_2O_4$,[8−10] and $LiMn_xNi_yCo_zO_2$,[11−15] exhibit insufficient specific capacity and energy density. Thus, it is vital to develop a high-energy cathode material. Li-excess-layered cathode (LLC) materials, often denoted as $(1-y)Li_2MnO_3{\cdot}yLiMO_2$ (M = Mn, Co, and Ni), have been described as either a composite or a solid solution of the rhombohedral $LiMO_2$ (R-3m space group) and monoclinic Li_2MnO_3 structures (C2/m space group). The rhombohedral $LiMO_2$ phase is composed of an octahedral transition metal (TM) oxide layer and an octahedral Li oxide layer, which are stacked repeatedly. The monoclinic Li_2MnO_3 phase can be written as $Li[Li_{1/3}Mn_{2/3}]O_2$ to allow the description of both structures as layered α-$NaFeO_2$-type rock-salt structures with cation ordering or long-range Li in-plane ordering and a $\sqrt{3}\,a_{hex} \times \sqrt{3}\,a_{hex}$ superstructure in the TM layer.[16,17]

These LLC materials have garnered much attention due to their high specific capacity, which exceeds 250 mAh g^{-1}[18−27] between 2.0 and 4.8 V.[28−31] This high specific capacity stems from two redox reactions: TM redox in the $LiMO_2$ component and oxygen anion redox reactions (O^{2-}/O_2^{n-}, $1 < n < 3$) in the Li_2MnO_3 component. The TM redox is known to have high reversibility but low capacity. On the other hand, the oxygen anion redox reaction is known to have a high capacity but low reversibility. The oxygen reaction causes unwanted phase transformations, leading to electrochemical performance fading. During the initial charge, TM oxidation occurs below 4.5 V vs Li/Li^+. Above 4.5 V vs Li/Li^+, oxygen oxidation occurs. During the oxygen oxidation process, various phase transformations occur, especially at the surface. Simultaneously, this process causes irreversible oxygen extraction and creates oxygen vacancies that lead to Mn migration from the TM layer to the Li layer. As a result, the $LiMn_2O_4$ spinel phase forms at the surface.[32] The formation of the $LiMn_2O_4$ spinel phase is detrimental to the battery performance because $LiMn_2O_4$ has lower Li diffusivity and lower electrical conductivity than the LLC. The Li diffusion coefficient is also lowered by the formation of incompatible phase boundaries between the spinel and layered phase and distortion of the diffusion channel at the phase boundaries.[33,34]

Received: April 9, 2020
Revised: May 3, 2020
Published: May 8, 2020

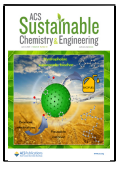

Thus, the discharge voltage decays over prolonged cycles. Furthermore, the spinel phase activates Mn redox by forming Mn^{3+} ions. The Mn^{4+}/Mn^{3+} redox reaction leads to severe Mn dissolution and Jahn−Teller distortion, causing a further phase transformation to the rock-salt phase, which is an electrochemically inactive and insulating phase. In a word, the formation of the $LiMn_2O_4$ spinel phase is one of the major causes of the low rate capability and the rapid capacity fading, which occurs during the cycling of the LLC.[35,36]

In an effort to overcome the issues associated with the $LiMn_2O_4$ spinel, recent works modified the surface of the LLC to form $Li_4Mn_5O_{12}$, a lithium-rich spinel/layered heterostructure, and admirably improved the electrochemical performance.[37−39] Compared to the $LiMn_2O_4$ spinel, this $Li_4Mn_5O_{12}$ spinel phase has less lattice mismatch with the host layered structure, which benefits the Li^+ ion diffusion rate.[40] Furthermore, the Mn in $Li_4Mn_5O_{12}$ has a higher oxidation state, Mn^{4+}, compared to that in the $LiMn_2O_4$ spinel, $Mn^{3.5+}$. This suggests that the $Li_4Mn_5O_{12}$ phase is significantly more stable in terms of Jahn−Teller distortion and dissolution than $LiMn_2O_4$. Even during the activation of the Mn redox, Mn^{4+} in the $Li_4Mn_5O_{12}$ only reduces down to $Mn^{3.4+}$.[41] The benefits of forming the $Li_4Mn_5O_{12}$ phase instead of the $LiMn_2O_4$ phase are clear. However, current methods of forming the $Li_4Mn_5O_{12}$ spinel phase are multistep surface synthesis,[36,39] which has high-cost, or one-step bulk synthesis,[37,38] which forms an excessive amount of spinel. Therefore, a one-step surface-selective method must be explored.

To overcome these limitations, various solutions have been proposed. Among various solutions, F^- anion doping is one of the most representative methods. By doping the F^- anion into the LLC, the spinel transformation is hindered through the formation of strong M-F bonding that impedes TM migration. Moreover, F^- has a higher oxidation state than the O^{2-} anion, lowering the oxidation state of TMs. Consequently, the reversible TM redox reaction capacity increases.[42−44] However, it has been shown that the F^- anion has a strong trapping effect on the polaron states in the lattice. Moreover, the mobility of the polaron states is lowered. Thus, F^- anion doping has a drawback in that it reduces the electrical conductivity of the LLC.[45] For this reason, alternative anion dopants such as N^{3-} and S^{2-} have been explored. The N^{3-} anion has a lower oxidation state than the O^{2-} anion, reducing the oxidation state of the TMs. In addition, N has lower electronegativity than O. Accordingly, the N^{3-} anion is oxidized before the O^{2-} anion to form N_2 gas, indicating that the N^{3-} anion is not a desirable dopant for the LLC. As an alternative, the S^{2-} anion can be doped into the LLC. Because the oxidation state of the S^{2-} anion is identical to that of the O^{2-} anion, it does not affect the oxidation state of TMs. Although S^{2-} can be oxidized before O^{2-} owing to the lower electronegativity, the S^{2-} anion forms solid elemental sulfur instead of undergoing the evolution of S gas at room temperature. Previous reports regarding sulfide-based electrode materials showed that S undergoes a reversible redox reaction during the charge/discharge process.[46−49] Park et al. and An et al. experimentally demonstrated that S^{2-} anion doping is beneficial for high specific capacity and reversible cycle retention in NCM and LLCs, respectively.[50,51] However, it should be noted that the dopant can deteriorate the specific capacity, rate capability, and average redox voltage. If overdoped or doped into the bulk of the LLC, S^{2-} can hinder Li-ion diffusion[52] and reduce the redox potential of the TM due to the lower electronegativity than oxygen ions, resulting in a lower energy density. For these reasons, it is necessary to investigate a method that retains a low concentration of the S^{2-} anion and mainly dopes only on the surface of the LLC to maximize the advantages and minimize the disadvantages. In addition, further analysis is also necessary to determine a mechanism by which the S^{2-} anion contributes to improving the electrochemical performance of S^{2-} anion-doped LLCs.

In this work, we propose a novel method by which to dope the S^{2-} anion onto the surface of the LLC selectively. The S-doped LLC demonstrates superior electrochemical performance in terms of the specific capacity, cycle retention, and rate capability relative to the corresponding outcomes for the LLC. The improved electrochemical performance of LLCs through the surface-selective S^{2-} anion doping is associated with the formation of the $Li_4Mn_5O_{12}$ spinel phase at the surface. Based on experimental analyses and first principles calculations, we elucidate the mechanisms of the S^{2-} anion during the surface phase transformation to the $Li_4Mn_5O_{12}$ spinel phase.

EXPERIMENTAL SECTION

Pristine LLC Synthesis. The LLC material, $Li_{1.2}Mn_{0.54}Ni_{0.13}Co_{0.13}O_2$, was synthesized using a solvothermal method followed by a heat treatment. Manganese acetate tetrahydrate ($Mn(CH_3COO)\cdot 4H_2O$), nickel acetate tetrahydrate ($Ni(CH_3COO)\cdot 4H_2O$), cobalt acetate tetrahydrate ($Co(CH_3COO)\cdot 4H_2O$), lithium hydroxide monohydrate ($LiOH\cdot H_2O$), and urea (CH_4N_2O) were used as precursors. $Mn(CH_3COO)\cdot 4H_2O$ (3.308 g), 0.808 g of $Ni(CH_3COO)\cdot 4H_2O$, 0.809 g of $Co(CH_3COO)\cdot 4H_2O$ (stoichiometric ratio of Mn:Ni:Co = 0.54:0.13:0.13), and 4.504 g of urea were dissolved in 50 mL of DI water with 25 mL of ethanol as a solvent under continuous stirring for 30 min. The prepared solution was moved into an 80 mL Teflon-lined autoclave. The autoclave was then kept in an oven at 200 °C for 10 h. After cooling to room temperature, the resultant was filtered and washed with ethanol and DI water at least three times and dried at 80 °C in a vacuum oven overnight to obtain the carbonate precursor. The prepared carbonate precursor and $LiOH\cdot H_2O$ (5% excess) were mixed, pressed into a pellet, calcined in a furnace at 500 °C for 6 h, and heated to 900 °C for 12 h at 5 °C min^{-1}. Subsequently, the LLC materials were obtained.

S-Doped LLC Synthesis. Surface sulfurization of the LLC materials was performed in a three-zone furnace with independent heating zones (Figure S1 in Supporting Information). Sulfur powder and the prepared LLC electrode were placed in the first and third heating zone (HT1 and HT3 in Figure S1), respectively. The mass ratio of the sulfur powder and the active material is presented in Table S1. Among the samples prepared with different sulfur ratios, S-LLC2 exhibited the best performance and will be denoted as "S-LLC" in the following results. The temperatures of the first (HT1), second (HT2), and third (HT3) heating zone was increased to 130, 140, and 350 °C, respectively, and held there for 1 h under flowing Ar gas at 1.5 L min^{-1}. All of the heating zones were then cooled to room temperature through a natural cooling process to obtain the S-doped LLC electrode (S-LLC).

Materials Characterization. The crystalline phase of LLC and S-LLC materials were identified by X-ray diffraction (XRD; Rigaku SmartLab) with a high-resolution powder X-ray diffractometer using Cu K_α (λ = 1.5418 Å) radiation. Elemental analysis of the synthesized materials was carried out using the inductive coupled plasma technique (ICP-OES; Agilent ICP-OES 5110). The morphology of the materials was observed with scanning electron microscopy (SEM; Phillips XL30) and high-resolution transmission electron microscopy (HRTEM; JEM-ARM200F) equipped with an energy dispersive spectrometry (EDS) detector. Raman spectroscopy (LabRAM HR Evolution, HORIBA Jobin Yvon) studies were performed before and after cycling the electrodes using a 514 nm laser. To prepare the

https://dx.doi.org/10.1021/acssuschemeng.0c02687
ACS Sustainable Chem. Eng. 2020, 8, 8037−8048

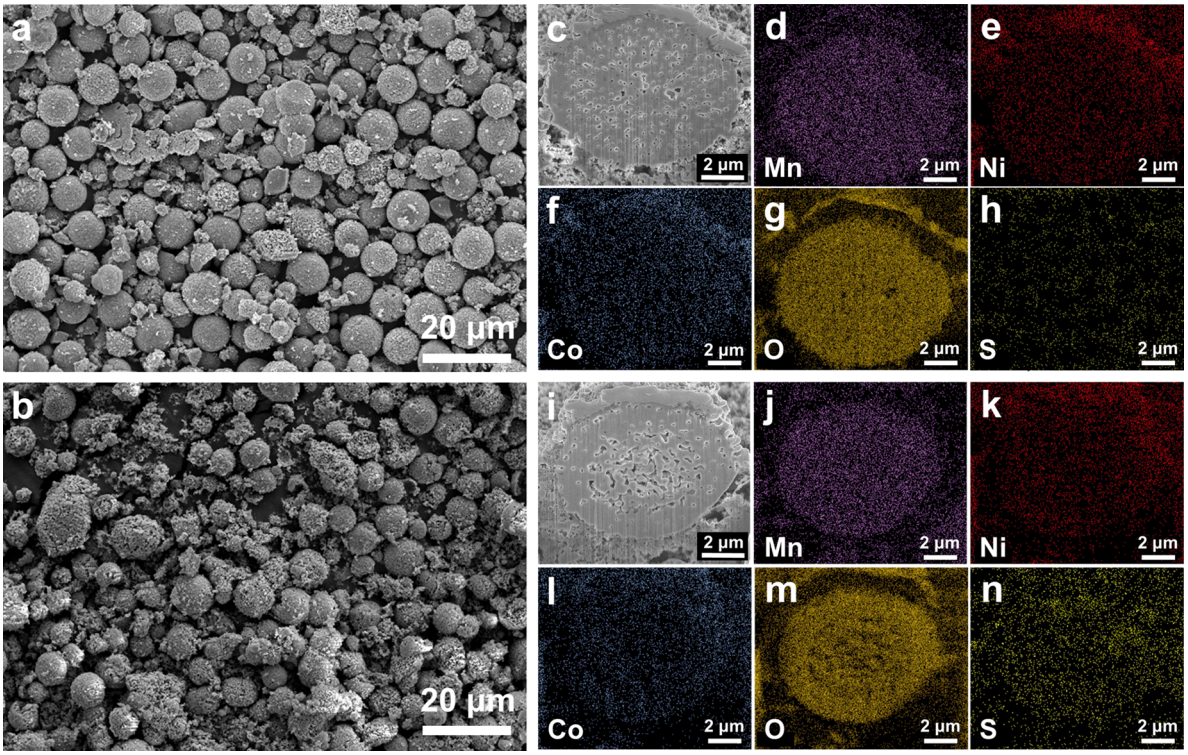

Figure 1. SEM images of (a) LLC and (b) S-LLC and (c, i) their corresponding cross-sectional images and EDS elemental mapping for (d, j) Mn, (e, k) Ni, (f, l) Co, (g, m) O, and (h, n) S.

cycled electrode samples for Raman spectroscopy, electrodes were sealed under argon between two slide glass slides with a Kapton tape in a glovebox. X-ray photoelectron spectroscopy (XPS; K-Alpha+ Thermo Fisher Scientific) was used to determine the ion valence states in the cathode materials. The depth profiles were obtained with etching the surface by an Ar ion beam with a 0.33 nm s^{-1} etching rate. The difference in the binding energy between the peaks (ΔE) of the Mn 3s region can be used to verify the average Mn oxidation state (AOS) by this equation; AOS = 8.956−1.126 ΔE.[53,54]

Electrochemical Measurement. The electrochemical properties of the prepared samples were measured using a 2032-type coin cell. The slurry was prepared by mixing 80 wt % of the active material ($Li_{1.2}Mn_{0.54}Ni_{0.13}Co_{0.13}O_2$), 10 wt % of conductive super P carbon, and 10 wt % of polyvinylidene fluoride (PVDF) as a binder in *N*-methyl-2-pyrrolidinone (NMP). The prepared slurry was cast on an Al foil current collector using the doctor-blade method and dried at 80 °C overnight in a vacuum oven. The loading mass of the active material was approximately 4−5 mg cm^{-2}. The electrolyte was prepared by mixing 1 M $LiPF_6$ in EC and 1 M $LiPF_6$ in a DEC solution at a 1:1 volume ratio. Electrochemical cycling tests of the prepared cells were performed in a voltage range of 2.0−4.8 V (vs Li^+/Li).

Computational Method. To explore the mechanisms of the S^{2-} anion during the surface phase transformation, we performed first principles calculations based on density functional theory (DFT) as implemented in the Vienna ab initio simulation package (VASP)[55] with the projector augmented-wave method to describe the valence electrons. The exchange-correlation functional was employed with the spin-polarized generalized gradient approximation (GGA) with the Perdew-Burke-Ernzerhof method.[56] To describe the onsite Coulomb interaction of the 3d state of Mn, we used Hubbard U correction[57] with the U_{eff} parameter taken from a previous report (U_{eff} = 5.0).[58] The antiferromagnetic (AF) arrangements of the spin on the Mn ions were also established in previous theoretical reports by Singh.[59] To mimic a low concentration of S-doping, we generated supercell structures with 12 and 8 unit cells for $LiMnO_2$ and Li_2MnO_3, respectively, and then replaced one oxygen atom with a S anion in each supercell to form $Li_{12}Mn_{12}O_{23}S_1$ and $Li_{16}Mn_8O_{23}S_1$, as illustrated in Figure S7. To evaluate the structural stability, we calculated the formation energy E_f defined by

$$E_f = E_T(\text{S} - \text{doped}) - E_T(\text{pristine}) - x\mu_S + x\mu_O, \quad (1)$$

where E_T(A) is the total energy of the layered system A, such as LiMnO2-xSx and Li2MnO3-xSx, representing "S-doped" with $x > 0$ and "pristine" with $x = 0$. Here, x is the number of substituted S atoms for O atoms within the unit cell, and μ_S and μ_O are the chemical potentials of S and O calculated as the O and S atoms in the gas-phase O2 and S8, respectively. The nudged elastic band (NEB) method was adopted to evaluate the diffusion energy barrier of the Mn ion along various migration pathways toward the layered-to-spinel phase transition.

RESULTS AND DISCUSSION

The morphologies of the LLC and S-LLC were observed by SEM (Figure 1a,b). Both samples (LLC and S-LLC) show spherical secondary particles with a diameter of 1 ∼ 10 μm, consisting of irregular primary particles with100 ∼ 200 nm in size (Figure 2a,g). The effects of sulfurization on the morphology and size of the primary and secondary particles were not distinctly observed. In contrast, ∼2 wt % of sulfur was detected only in the S-LLC by an EDS analysis. The composition ratios of Mn:Ni:Co in the LLC as measured by EDS and ICP were 0.54:0.13:0.13 and 0.543:0.133:0.131, respectively. Cross-sectional SEM images of the LLC and S-LLC and their corresponding EDS elemental mappings for Mn, Ni, Co, O, and S are provided (Figure 1c−h, i−n). The TMs and oxygen are uniformly distributed throughout the secondary particles of the LLC and S-LLC. In the S-LLC, S is also uniformly distributed throughout the secondary particles, reflecting that S was doped not only into the surface of the secondary particles but also into the surface of the primary particles throughout the secondary particles.

https://dx.doi.org/10.1021/acssuschemeng.0c02687
ACS Sustainable Chem. Eng. 2020, 8, 8037−8048

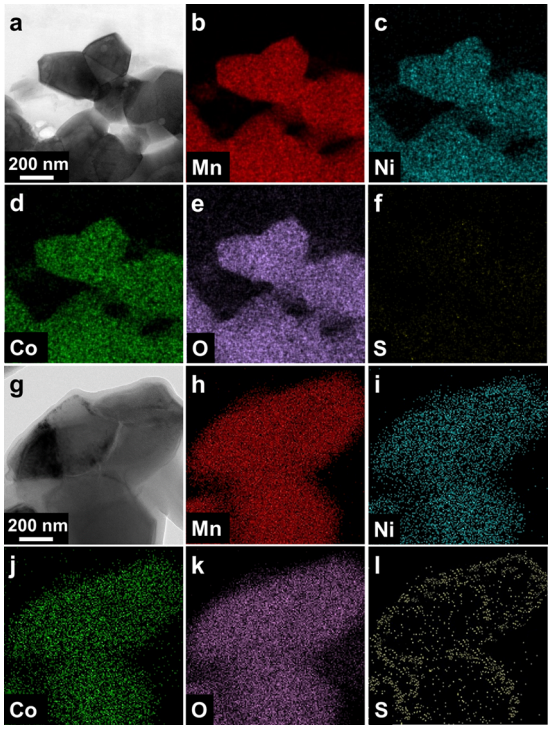

Figure 2. (a, g) HRTEM images and (b–f, h–l) corresponding EDS elemental mappings of the LLC and S-LLC samples.

To investigate the structure of the LLC and S-LLC, HRTEM images were obtained (Figure S2a,b). Both LLC and S-LLC exhibited the well-ordered atomic arrangements with a lattice spacing of 4.7 Å that correspond to the (003) plane and (002) plane of R-3m- and C2/m-layered structures of the cathode materials, respectively. Although S^{2-} has a larger ionic radius (1.84 Å) than O^{2-} (1.4 Å), the S-LLC does not show a significant difference in the interlayer distance due to the low S concentration (~2 wt %). The elemental distributions of the primary particles of the LLC and S-LLC were examined using HRTEM (Figure 2), and its corresponding EDS spectra and results are shown in Figure S3 and Table S2. Mn, Ni, Co, and O are uniformly distributed in the primary particles. Only in the S-LLC S signals were observed, mainly at the surface of the primary particles. S signals detected in the middle of the primary particle imply that the S-doping suitably covers the entire surface of the primary particles. These results indicate the significant merit of the sulfurization method proposed in this study. If S is overdoped or doped into the bulk of the particles, it is expected to hinder Li^+ ion diffusion.[60] Thus, to improve the electrochemical performance, a small amount of S should be doped locally onto the surface. Furthermore, using the proposed method, S is doped not only onto the surfaces of the secondary particles but also onto the surfaces of the primary particles through the secondary particles (Figures 1n and 2l). Accordingly, S-doping can more effectively improve the electrochemical performance of the LLC.

To examine the effects of S-doping on the crystal structure, XRD patterns are obtained for the LLC and S-LLC (Figure 3a). The main diffraction peaks indicate that both materials have the typical hexagonal-layered phase (space group: R-3m) corresponding to the α-$NaFeO_2$ structure. The weak superlattice peaks in the 2θ range of 20–25° stemmed from the monoclinic Li_2MnO_3 (space group: C2/m) phase in both materials. For the quantitative analysis of the lattice parameter, Rietveld refinement is performed and shown in Figure S4. The calculated lattice parameters are presented in Table S3. Rietveld refinement results reflect that S-doping has negligible effects on the crystal structure of the LLC. Considering that

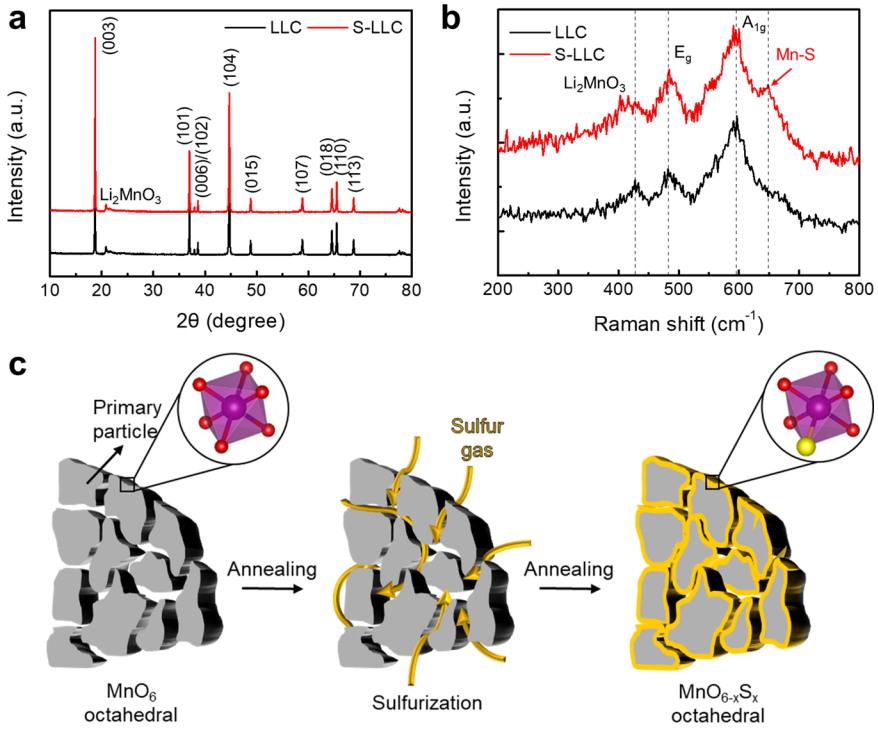

Figure 3. (a) XRD patterns and (b) Raman spectra of the LLC and S-LLC. (c) Schematic illustration of the surface sulfurization process of the S-LLC. Sulfur gas diffuses through the voids in the secondary particles of the LLC and substitutes for O on the surfaces of the primary particles.

https://dx.doi.org/10.1021/acssuschemeng.0c02687
ACS Sustainable Chem. Eng. 2020, 8, 8037–8048

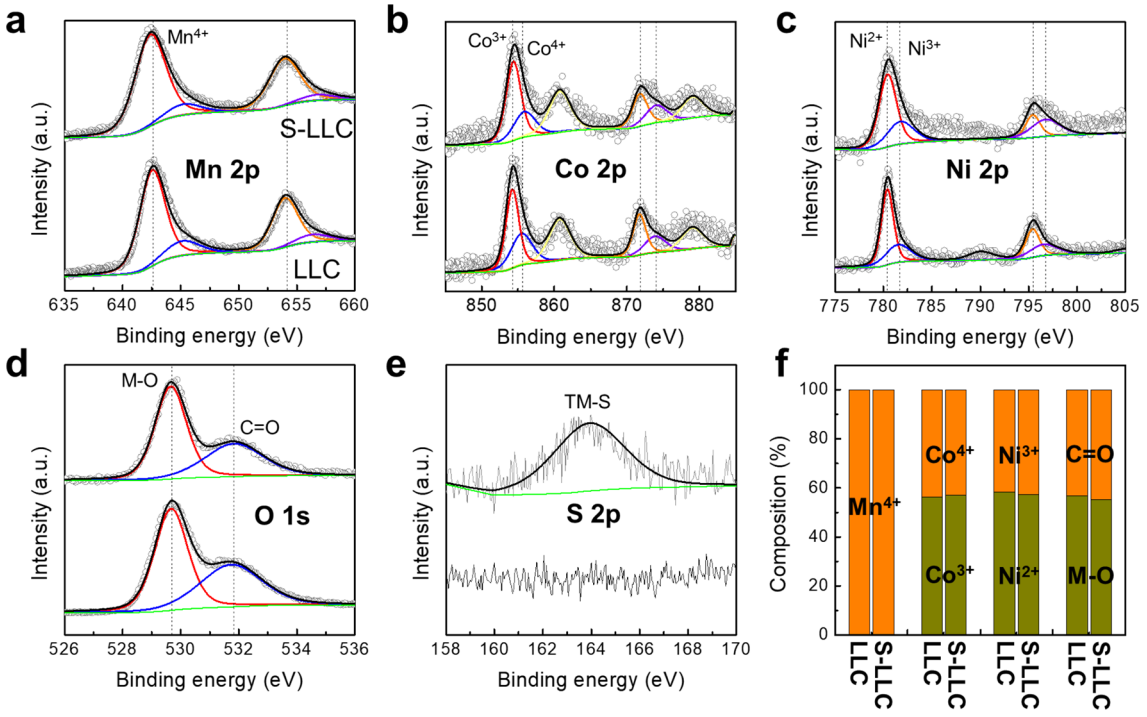

Figure 4. XPS spectra of (a) Mn 2p, (b) Co 2p, (c) Ni 2p, (d) O 1s, and (e) S 2p of the LLC and S-LLC, and (f) the corresponding peak intensity ratio for each component.

XRD is largely a bulk technique and that doped S is mainly distributed on the surfaces of the primary particles, surface-focused analyses must be conducted to identify the structural differences arising from S-doping.

The Raman spectra (Figure 3b) indicate that the LLC and S-LLC have two broad bands at 493 and 605 cm^{-1}, indicating the E_g and A_{1g} vibrational modes of the R-3m-layered structure.[61] Additionally, a weak and broad vibrational mode at around 400 cm^{-1}, corresponding to the C2/m space group (Li_2MnO_3), is also observed in both samples. Unlike the LLC, a clear shoulder peak at 648 cm^{-1} appears for the S-LLC sample. This shoulder peak indicates the vibrational mode resulting from the Mn-S bonds,[62,63] clearly confirming that S was doped into the LLC to form Mn-S bonds in the S-LLC through sulfurization. Figure 3c shows a schematic illustration of the surface sulfurization process. The S gas penetrates throughout the entire secondary particle after which the S^{2-} anion replaces the O^{2-} anion on the crystal lattice of the LLC from the surfaces of the primary particles. This results in S-doping throughout the surface of the primary particles on the atomic level.

To investigate the effects of S-doping on the oxidation states of the components, XPS analyses were conducted. The chemical compositions of the LLC and S-LLC obtained from the XPS spectra are illustrated in Figure S5a. Figure 4a displays the Mn $2p_{3/2}$ and $2p_{1/2}$ main and satellite peaks. Both samples have a peak at 642.6 eV corresponding to Mn^{4+} $2p_{3/2}$. Figure 4b displays the Co $2p_{3/2}$ and $2p_{1/2}$ main and satellite peaks. Both samples have Co^{3+} $2p_{3/2}$ and Co^{4+} $2p_{3/2}$ peaks located at 854.3 and 855.6 eV, respectively. Figure 4c displays the Ni $2p_{3/2}$ and $2p_{1/2}$ main and satellite peaks. Both samples have Ni^{2+} and Ni^{3+} peaks located at 780.4 and 781.7 eV, respectively. Figure 4d displays the O 1s spectra. The peaks observed at 529.7 and 531.8 eV are attributed to lattice oxygen (M−O) and Li_2CO_3 (C═O), respectively. Li_2CO_3 can be found on layered oxide cathodes due to the reaction with moisture and CO_2 during storage.[64] From the data shown in Figure 4a−d, the compositions of each species are calculated for the LLC and S-LLC (Figure 4e). Sulfurization does not change the valence states of TMs (Mn, Ni, and Co) because the oxidation state of the oxidation state S^{2-} anion is identical to that of the O^{2-} anion. Additionally, the ratio of M-O and C═O remains unchanged during the sulfurization step. Figure 4f displays the S 2p signal. As expected, the S 2p peak is observed only in the S-LLC sample at 163.8 eV, indicative of a TM-S species.[65,66] Furthermore, the depth profile of the S-LLC results also indicates the surface selectively existence of the S^{2-} anion (Figure S5b,c). From these results, it can be considered that the S^{2-} anion in the S-LLC is successfully doped to the oxygen site and bonded with the Mn ion; especially, this phenomenon occurs at the surface. Furthermore, as expected, the S^{2-} anion does not alter the valence states of other elements. The influence of surface S-doping on the electrochemical performance outcomes is discussed below.

Figure 5a,b presents the charge−discharge curves for the LLC and S-LLC measured at the 1st, 25th, 50th, 100th, and 200th cycle. The initial discharge capacity of the LLC and S-LLC is 240.45 and 231.74 mAh/g, respectively. As the cycling process continues, the LLC and S-LLC both exhibit a similar degree of average discharge voltage decay. However, in terms of the specific capacity, the S-LLC shows much slower degradation than the LLC; the specific capacity of S-LLC remains even higher than the initial value up to 100 cycles. Figure 5c exhibits the charging and discharging cycle capacities and Coulombic efficiency of the LLC and S-LLC measured at 0.1 C (1 C = 250 mA/g). The discharge capacity of the LLC decreases from 240.45 to 176.42 mAh/g after 200 cycles, corresponding to a cycle retention of 73.4%. The S-LLC shows considerably improved cycle performance for 200 cycles. The

https://dx.doi.org/10.1021/acssuschemeng.0c02687
ACS Sustainable Chem. Eng. 2020, 8, 8037−8048

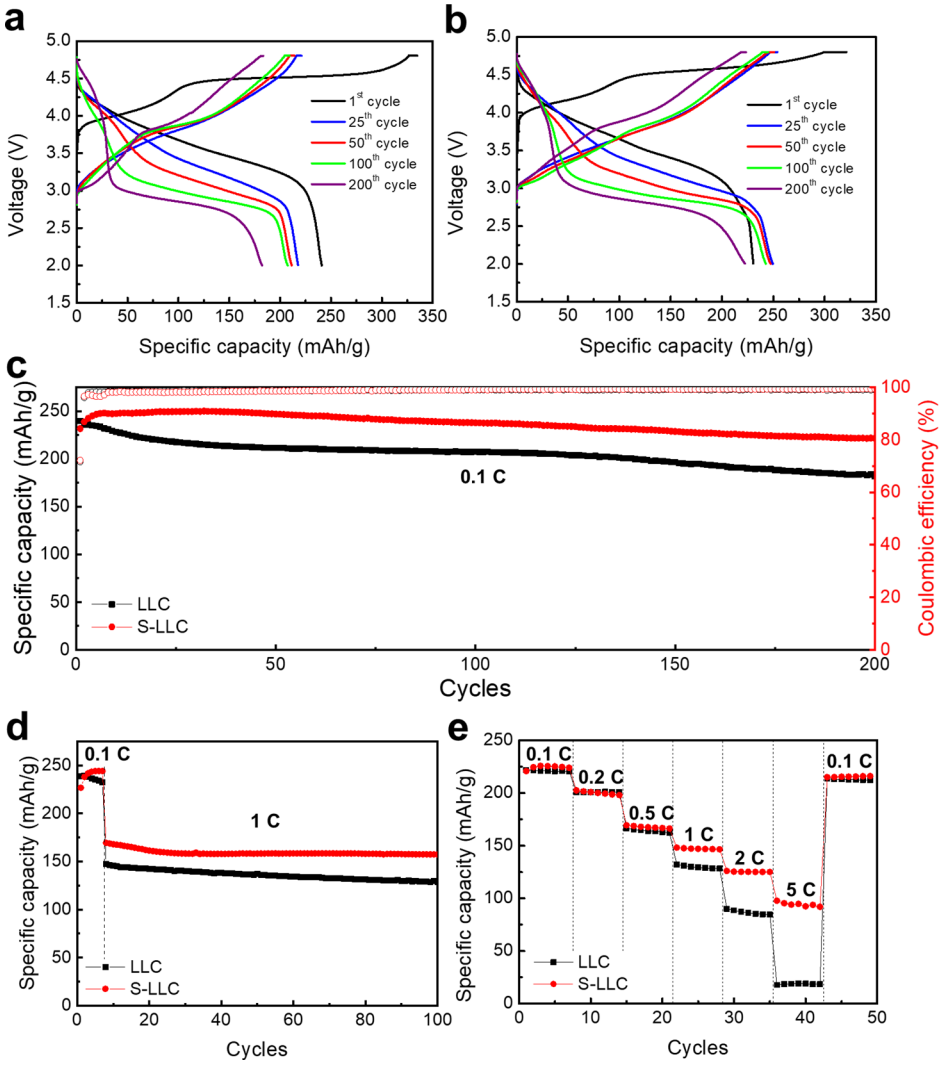

Figure 5. Charge−discharge curves at the 1st, 25th, 50th, 100th, and 200th cycle of (a) LLC and (b) S-LLC samples. (c) Cycling performance outcomes of the LLC and S-LLC samples over 200 cycles at the 0.1 C rate and (d) over 100 cycles at the 1 C rate. (e) Rate capability outcomes of the LLC and S-LLC samples.

initial discharge capacity of S-LLC is 231.74 mAh/g and decreases to 220.62 mAh/g with a capacity retention of 95.2%.

One of the advantages of the sulfurization method proposed in this study is that the amount of S-doping can be finely controlled simply by changing the amount of S powder. The exact number of samples prepared with different S ratios loaded in HT1 is summarized in Table S1, and the corresponding chemical compositions of the samples are summarized in Table S4. As shown in Figure S6, when the S content is 0.12 wt % (S-LLC1), the electrochemical performance of the LLC and S-LLC1 are similar. On the other hand, when the S content is 4.32 wt % (S-LLC3), initial specific capacity is reduced, likely because the overdoped S hinders Li^+ ion diffusion. The cycling performance also deteriorates. Among the prepared samples, the 2.20 wt % S-doped LLC (S-LLC2) demonstrated an improved initial specific capacity and better cycling stability. Unless specified, the S-doped LLC in this study contains 2.20 wt % of S.

The cycling stability outcomes of both samples at a high rate (1 C) are shown in Figure 5d. A high rate test is performed after seven cycles at a low rate (0.1 C) for activation. After 100 cycles at a high rate, the LLC sample exhibits relatively poor cycle retention of 85.8%, whereas the S-LLC sample shows a better cycle retention of 92.1%. Figure 5e shows the rate performance of both the samples when the current rate ranges from 0.1 to 5 C. Both the LLC and S-LLC show similar discharge capacities at the low rates of 0.1 and 0.2 C. However, as the current rate increases, the discharge capacities of both the samples show significant differences; the discharge capacities of the LLC and S-LLC measured at 1C are 128.26 and 146.60 mAh/g, respectively, while the corresponding values measured at 5 C are 18.41 and 92.03 mAh/g. These results demonstrate that the S-LLC can deliver a much higher discharge capacity at a higher current rate compared to the LLC. Although doped S can even hinder Li^+ ion diffusion and deteriorate the electrochemical performances, the S-doping conducted in this study remarkably improves not only the cycling retention but also the rate capability. In addition to the confinement of the doped S to the surface, other factors can contribute to the improvement of the rate performance, as addressed below.

The differential capacity displays fine differences in the redox processes between the LLC and S-LLC. As shown in Figure 6a, both the samples show similar initial differential

https://dx.doi.org/10.1021/acssuschemeng.0c02687
ACS Sustainable Chem. Eng. 2020, 8, 8037−8048

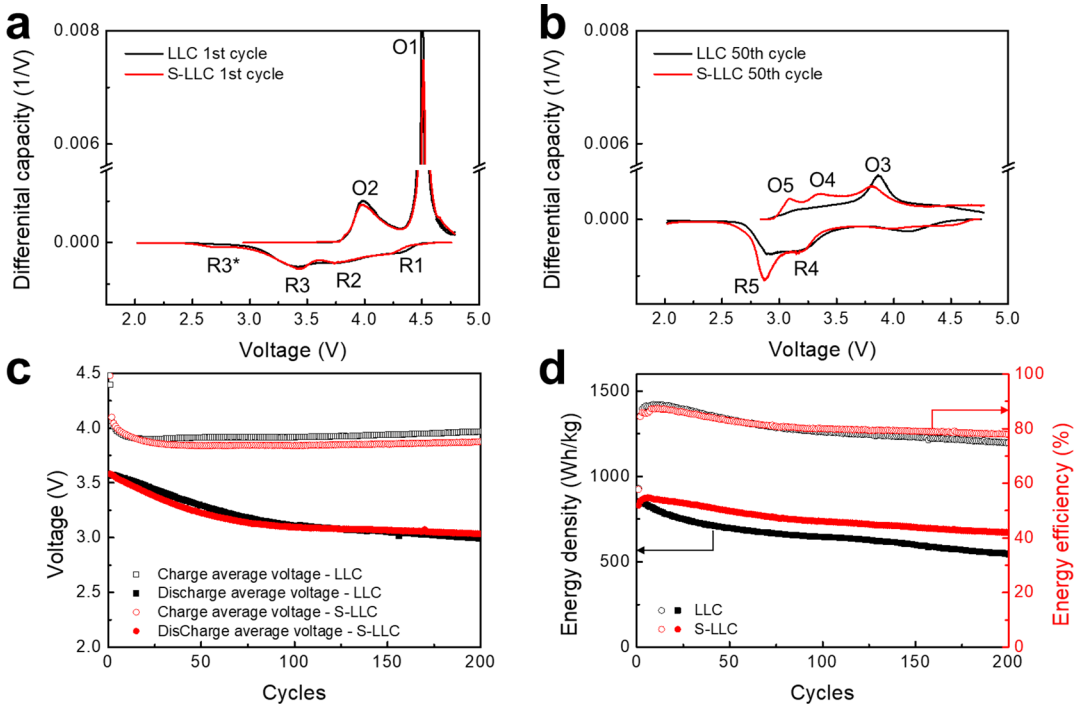

Figure 6. Differential capacity plots for (a) 1st and (b) 50th cycles of the LLC and S-LLC, and (c) charge/discharge average voltage and (d) energy density and efficiency of the LLC and S-LLC samples.

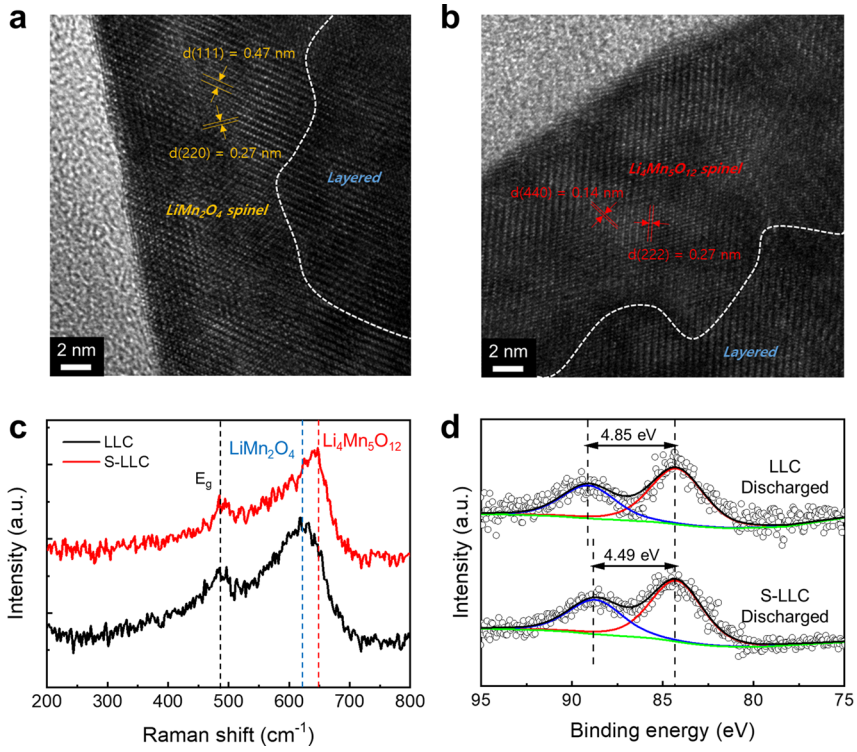

Figure 7. HRTEM images of (a) LLC and (b) S-LLC and, (c) Raman spectra and (d) XPS Mn 3s regions of the LLC and S-LLC after 50 cycles at the 0.1 C rate.

capacity curves. The first charging process consists of two oxidation reactions: (1) Li^+ extraction from the layered structure of $LiMO_2$ at 4.0 V (O2) with the oxidation reactions of Co^{3+}/Co^{4+} and Ni^{2+}/Ni^{4+} and (2) partially irreversible Li^+ extraction from the Li_2MnO_3 component at 4.5 V (O1) with the anionic oxidation reactions of O^{2-}/O_2^{n-} ($1 < n < 3$). The O1 and O2 peaks correspond to the R1 (4.3 V) and R2 (3.7 V) reduction reactions, respectively. The reduction peak at 3.4 V (R3) associated with Mn^{4+}/Mn^{3+} occurs after the activation process caused by the O1 reaction. After activated the Mn ion migrates to the Li layer, spinel phases are formed at the surface during the first few cycles. Lastly, the reduction peak at 2.8 V

https://dx.doi.org/10.1021/acssuschemeng.0c02687
ACS Sustainable Chem. Eng. 2020, 8, 8037−8048

(R3*) is observed only in the S-LLC. R3 and R3* are formed by the Mn reaction of the spinel phase.[67] However, unlike R3, R3* is often more pronounced after a few cycles of spinel formation. Thus, the appearance of R3* even in the initial cycle suggests that the spinel formed in the S-LLC is significantly more redox active.

To compare the redox reactions of the fully developed spinel phase, differential capacity is analyzed after 50 cycles (Figure 6b). The LLC and S-LLC demonstrate similar differential curves. The anodic peaks appearing between 3.5 and 4.0 V (O3) are associated with Co^{3+}/Co^{4+} and Ni^{2+}/Ni^{4+}, corresponding to broad cathodic peaks between 3.5 and 4.5 V. Two reduction peaks (R4 and R5), which appear between 2.5 and 3.4 V, are generated by the reduction of Mn^{4+}/Mn^{3+}.[68,69] The peaks at 3.2 V (R4) are ascribed to a layered structure with a number of spinel-like compositions, whereas the peaks at 2.8 V (R5) are identical to those associated with Mn spinel reduction. The oxidation peaks at 3.3 V (O4) and 3.1 V (O5) correspond to the R4 and R5 reduction reactions, respectively.[70] The lower shift of the Mn^{4+}/Mn^{3+} reduction peak has been attributed to the structural transformation from the layered phase to the spinel phase, which is mainly caused by TM ion migration.[40] One of the striking differences between the LLC and S-LLC is the amplitude of Mn redox peaks, R5 and O5. The S-LLC displays significantly more pronounced Mn redox peaks, indicating that the S-LLC has superior reversibility of the Li insertion/extraction process and the spinel Mn redox reaction. Figure 6c shows the average charge/discharge voltage of both samples throughout the cycles. After 200 cycles, the S-LLC shows a slightly higher average discharge voltage than the LLC, and interestingly, average charge voltage is clearly enhanced than the LLC. The lower average discharge voltage of the S-LLC compared to that of the LLC during the initial 100 cycles is likely due to the fact that the S-LLC gains more capacity from the low-voltage spinel discharge reaction. From the data in Figures 6c and 5a,b, the energy density during the cycling process is calculated (Figure 6d). As mentioned above, the S-LLC has a slightly higher average discharge voltage, a lower average charge voltage, and an even higher capacity after cycling due to the reversible Mn redox reaction in the low-voltage region, resulting in a higher overall discharge energy density than the LLC. The initial energy densities of the LLC and S-LLC are 854.9 and 830.5 Wh/kg, respectively. After 200 cycles, the energy densities of the LLC and S-LLC are 554.0 and 672.1 Wh/kg, respectively. Additionally, due to the higher average charge voltage and higher charge capacity of the S-LLC, the S-LLC also shows a higher charge energy density. More importantly, because the higher charge energy density is resulted from the stable low charge voltage region, the energy efficiency of the S-LLC during cycling is improved by 3.1% compared to that of the LLC. From these results, we can postulate that the S^{2-} anion in the lattice still forms the surface spinel, but it affects the transformation in a positive manner.

To investigate the effects of the charge/discharge cycles on the surface phase of the LLC and S-LLC, HRTEM analyses of both samples are demonstrated (Figure 7a,b). The HRTEM images show that both samples have a spinel phase in the surface region and a layered phase in the bulk region. However, the surface of the LLC is mainly composed by the $LiMn_2O_4$ spinel phase with corresponding d-spacing,[71,72] and the surface of the S-LLC is mainly constructed by the $Li_4Mn_5O_{12}$ spinel phase with corresponding d-spacing.[37,38,61,73] The atomic arrangement of both spinel phases is quite similar since it depends on whether Li ions occupy the Mn sites (Figure S8b,d), so further evidences are needed to specify the each spinel phases.

Raman spectroscopy is also conducted after 50 cycles (Figure 7c). The vibrational modes corresponding to the layered structures observed in the pristine LLC and S-LLC (E_g and A_{1g} in Figure 3b) have been eliminated due to the surface phase transformation caused by Mn migration. The vibrational mode of the spinel phase is dominant in both the LLC and S-LLC spectra with small E_g peaks from the layered phase. However, the peak positions of the main vibrational modes (A_{1g}) of the LLC and S-LLC shift differently, meaning that both samples transform into a spinel structure but have different spinel structures. The main broad band at 623 cm^{-1} for the LLC is evidence of $LiMn_2O_4$,[74] a well-known spinel structure generally induced by a layered-spinel phase transition. On the other hand, the main vibrational mode of the S-LLC at 649 cm^{-1} indicates the $Li_4Mn_5O_{12}$ spinel phase.[75]

For a more in-depth investigation of the oxidation states of the spinel phase, an Mn 3s XPS analysis was conducted after 50 cycles (Figure 7d). The Mn 3s peaks are split into two signals due to the coupling of the nonionized 3s electron with 3d valence-band electrons.[76] The magnitude of peak splitting is diagnostic of the Mn oxidation state. The peak splitting outcomes for the LLC and S-LLC are 4.85 and 4.49 eV, respectively. They correspond to the average oxidation state of $Mn^{3.49+}$ and $Mn^{3.90+}$, respectively. The Mn oxidation state also supports the contention that the surface of the LLC transforms into the $LiMn_2O_4$ spinel phase and that the S-LLC transforms into the $Li_4Mn_5O_{12}$ spinel phase. Compared to the $LiMn_2O_4$ spinel transformation, the $Li_4Mn_5O_{12}$ spinel transformation results in a better cycling stability owing to the smaller lattice mismatching, the mitigated Jahn−Teller effect, the suppressed Mn dissolution, and hence the improved structural stability.[40,77−80] Ultimately, $Li_4Mn_5O_{12}$ has the higher Li^+ ion diffusivity and electrical conductivity,[41,81−84] explaining why the S-LLC with $Li_4Mn_5O_{12}$ shows a better cycling retention and rate capability than the LLC with $LiMn_2O_4$.

To understand the phase transition from the layered LLC and S-LLC at the delithiated state toward their spinel counterparts, we investigated Mn migrations using first principles DFT calculations. It is well known that during the charge/discharge process, a $LiMnO_2$-layered structure (Figure S8a) can be converted to its corresponding $LiMn_2O_4$ spinel structure (Figure S8b) by Mn ion migration. Similarly, Mn ion migration leads the phase transition from a Li_2MnO_3 Li-excess-layered structure (Figure S8c) to its corresponding $Li_4Mn_5O_{12}$ spinel structure (Figure S8d). In the Li-excess compositions, additional Li ions are located inside TM layers. In addition, to scrutinize the effects of S-doping on the phase transition, we evaluated the structural stability and the migration process of Mn ions in the S-doped materials. Using eq 1, the formation energies of S-doped layered materials, $Li_{12}Mn_{12}O_{23}S_1$ and $Li_{16}Mn_8O_{23}S_1$, were calculated to be −0.56 and − 0.39 eV, respectively, indicating that both the S-doped structures are thermodynamically favorable and thus S-doping may occur naturally.

During the delithiation process, some of the Mn ions in either pristine or S-doped layered material begin to migrate toward the Li layers from the TM layers, which initiates the phase transition to the spinel counterpart. To mimic the delithiation process, we removed 50% of Li ions from each of

https://dx.doi.org/10.1021/acssuschemeng.0c02687
ACS Sustainable Chem. Eng. 2020, 8, 8037−8048

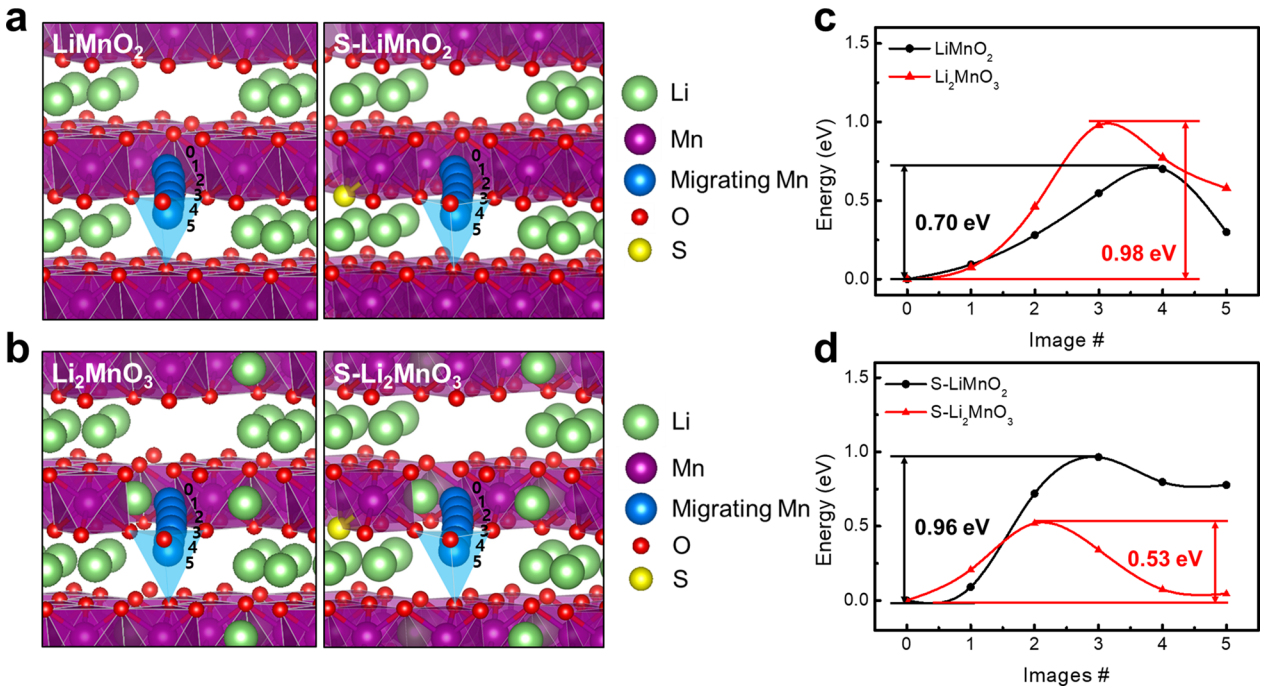

Figure 8. Pathways of the Mn migration position of pristine (left) and S-doped (a) $LiMnO_2$ and (b) Li_2MnO_3, respectively. Energy barriers of the Mn migration pathway in (c) pristine and (d) S-doped cases. The black (red) lines indicate either pristine or S-doped $LiMnO_2$ (Li_2MnO_3).

the layered structures. These Li vacancies provide sufficient rooms for each Mn ion to migrate from the TM layer. Figure 8a,b illustrates the Mn migration paths from an octahedral site of the TM layer toward a neighboring tetrahedral site (blue tetrahedron) of the Li layer. For these migration paths, we estimated the migration energy barriers using the NEB method and presented them in Figure 8c,d, where black lines represent both pristine or S-doped $LiMnO_2$ and red ones for Li_2MnO_3. For the pristine case, the Mn migration energy barrier in $LiMnO_2$ was calculated to be ~0.70 eV, which is smaller by ~0.28 eV than that in Li_2MnO_3 as shown in Figure 8c, indicating that the $LiMn_2O_4$ spinel transformed from the $LiMnO_2$ layer would exist dominantly on the LLC surface. For the S-doped case, there are inequivalent Mn ions that participate in the migration process depending on their relative positions to the doped S atom. Considering that the concentration of doped S is very low as demonstrated above, we selected the Mn ion, which is not directly connected to the S atom, for the migration process. Figure 8d shows the migration energy barriers of the Mn ions in the S-doped $LiMnO_2$ (black lines) and Li_2MnO_3 (red lines), which are about 0.96 and 0.53 eV, respectively. Compared to the results for the pristine case, the S-doping increases the Mn migration barrier by 0.26 eV in $LiMnO_2$, while the S-doping intriguingly reduces the barrier by 0.45 eV in Li_2MnO_3, implying that it is more likely to form a $Li_4Mn_5O_{12}$ spinel phase from the Li_2MnO_3 structure on the S-LLC surface. The formation of the $Li_4Mn_5O_{12}$ spinel phase contributes the improvement of cycle life because of its high oxidation state of Mn than that of $LiMn_2O_4$, and the high oxidation state of Mn can resist structural distortion caused by lattice mismatching, the Jahn–Teller effect, and dissolution during the charge/discharge process.

CONCLUSIONS

In this work, we improve the electrochemical performances of an LLC material ($Li_{1.2}Mn_{0.54}Ni_{0.13}Co_{0.13}O_2$) through a surface sulfurization method. S is selectively doped on the surfaces of the primary particles of the LLC. The prepared S-doped LLC (S-LLC) shows more stable cycle retention and rate performance than the LLC. The S-LLC also shows enhanced energy efficiency due to the stable average charge voltage than the LLC. As the main reason for good cycle retention, it is confirmed that S-doping leads to the formation of the $Li_4Mn_5O_{12}$ spinel phase on the surface as opposed to the $LiMn_2O_4$ spinel phase. This $Li_4Mn_5O_{12}$ spinel phase, unlike the conventional $LiMn_2O_4$ spinel, has more favorable Li^+ ion diffusion and electrical conductivity with regard to the material. This $Li_4Mn_5O_{12}$ phase transformation is a key for the cathode materials to maintain good cycling stability because the stable Mn ions can resist the structural distortion caused by lattice mismatching, the Jahn–Teller effect, and dissolution. This work demonstrates that the S-doping selectively lowers the Mn migration barrier of the Li_2MnO_3 structure that leads to the formation of the $Li_4Mn_5O_{12}$ spinel phase in the S-LLC. It should be pointed out that this work opens up S-doping as a viable solution for various cathode materials associated with the surface spinel formation issue. Furthermore, this work demonstrates that there are anions other than F^- that also should be explored.

ASSOCIATED CONTENT

Supporting Information

The Supporting Information is available free of charge at https://pubs.acs.org/doi/10.1021/acssuschemeng.0c02687.

Schematic experimental process, TEM images, XRD patterns, charge/discharge profiles, and model structures of DFT calculation (PDF)

https://dx.doi.org/10.1021/acssuschemeng.0c02687
ACS Sustainable Chem. Eng. 2020, 8, 8037–8048

AUTHOR INFORMATION

Corresponding Authors

Young-Kyun Kwon − *Department of Physics and Research Institute for Basic Sciences, Kyung Hee University, Seoul 02447, Korea;* orcid.org/0000-0001-6027-8408; Email: ykkwon@khu.ac.kr

Jaewook Shin − *Department of Materials Science and Engineering and Advanced Battery Center, KAIST Institute for NanoCentury, Korea Advanced Institute of Science and Technology, Daejeon 34141, Korea;* orcid.org/0000-0002-7431-9255; Email: jashin@kaist.ac.kr

EunAe Cho − *Department of Materials Science and Engineering and Advanced Battery Center, KAIST Institute for NanoCentury, Korea Advanced Institute of Science and Technology, Daejeon 34141, Korea;* orcid.org/0000-0002-2871-6903; Email: eacho@kaist.ac.kr

Authors

Yongju Lee − *Department of Materials Science and Engineering, Korea Advanced Institute of Science and Technology, Daejeon 34141, Korea*

Tae-Hee Kim − *Department of Materials Science and Engineering, Korea Advanced Institute of Science and Technology, Daejeon 34141, Korea;* orcid.org/0000-0003-0209-2423

Complete contact information is available at: https://pubs.acs.org/10.1021/acssuschemeng.0c02687

Notes

The authors declare no competing financial interest.

ACKNOWLEDGMENTS

The authors would like to thank the characterization facility in the Department of Materials Science and Engineering at KAIST, KAIST Analysis Center for Research Advancement, and National Nanofab Center for granting assess to their equipment. This work was supported by the National Research Foundation of Korea (NRF) (2018006908) and is based on a research, which has been conducted as part of the KAIST-funded Global Singularity Research Program for 2019.

REFERENCES

(1) Tarascon, J. M.; Armand, M. Issues and Challenges Facing Rechargeable Lithium Batteries. *Nature* **2001**, *414*, 359−367.

(2) Zheng, Z.; Li, P.; Huang, J.; Liu, H.; Zao, Y.; Hu, Z.; Zhang, L.; Chen, H.; Wang, M.-S.; Peng, D.-L.; Zhang, Q. High Performance Columnar-like Fe2O3@carbon Composite Anode via Yolk@shell Structural Design. *J. Energy Chem.* **2020**, *41*, 126−134.

(3) Maram, P. S.; Costa, G. C. C.; Navrotsky, A. Experimental Confirmation of Low Surface Energy in LiCoO2 and Implications for Lithium Battery Electrodes. *Angew. Chem. Int. Ed.* **2013**, *52*, 12139−12142.

(4) Sakuda, A.; Nakamoto, N.; Kitaura, H.; Hayashi, A.; Tadanaga, K.; Tatsumisago, M. All-Solid-State Lithium Secondary Batteries with Metal-Sulfide-Coated LiCoO2 Prepared by Thermal Decomposition of Dithiocarbamato Complexes. *J. Mater. Chem.* **2012**, *22*, 15247−15254.

(5) Yuan, L. X.; Wang, Z. H.; Zhang, W. X.; Hu, X. L.; Chen, J. T.; Huang, Y. H.; Goodenough, J. B. Development and Challenges of LiFePO4cathode Material for Lithium-Ion Batteries. *Energy Environ. Sci.* **2011**, *4*, 269−284.

(6) Shi, Q.; Xue, L.; Wei, Z.; Liu, F.; Du, X.; DesMarteau, D. D. Improvement in LiFePO4-Li Battery Performance via Poly(Perfluoroalkylsulfonyl)Imide (PFSI) Based Ionene Composite Binder. *J. Mater. Chem. A* **2013**, *1*, 15016−15021.

(7) Wang, J.; Yang, J.; Tang, Y.; Li, R.; Liang, G.; Sham, T. K.; Sun, X. Surface Aging at Olivine LiFePO4: A Direct Visual Observation of Iron Dissolution and the Protection Role of Nano-Carbon Coating. *J. Mater. Chem. A* **2013**, *1*, 1579−1586.

(8) Wang, J.; Zhang, Q.; Li, X.; Wang, Z.; Guo, H.; Xu, D.; Zhang, K. Sputtering Graphite Coating to Improve the Elevated-Temperature Cycling Ability of the LiMn2O4 Electrode. *Phys. Chem. Chem. Phys.* **2014**, *16*, 16021−16029.

(9) Guan, D.; Jeevarajan, J. A.; Wang, Y. Enhanced Cycleability of LiMn2O4 Cathodes by Atomic Layer Deposition of Nanosized-Thin Al2O3 Coatings. *Nanoscale* **2011**, *3*, 1465−1469.

(10) Dai, Y.; Cai, L.; White, R. E. Capacity Fade Model for Spinel LiMn2O4 Electrode. *J. Electrochem. Soc.* **2012**, *160*, A182−A190.

(11) Schougaard, S. B.; Bréger, J.; Jiang, M.; Grey, C. P.; Goodenough, J. B. LiNi0.5+δMn0.5-ΔO2-a High-Rate, High-Capacity Cathode for Lithium Rechargeable Batteries. *Adv. Mater.* **2006**, *18*, 905−909.

(12) Wang, Y.; Cao, G. Developments in Nanostructured Cathode Materials for High-Performance Lithium-Ion Batteries. *Adv. Mater.* **2008**, *20*, 2251−2269.

(13) Jung, S. K.; Gwon, H.; Hong, J.; Park, K. Y.; Seo, D. H.; Kim, H.; Hyun, J.; Yang, W.; Kang, K. Understanding the Degradation Mechanisms of LiNi0.5Co0.2Mn0.3O2 Cathode Material in Lithium Ion Batteries. *Adv. Energy Mater.* **2014**, *4*, 1300787.

(14) Wei, Y.; Zheng, J.; Cui, S.; Song, X.; Su, Y.; Deng, W.; Wu, Z.; Wang, X.; Wang, W.; Rao, M.; Lin, Y.; Wang, C.; Amine, K.; Pan, F. Kinetics Tuning of Li-Ion Diffusion in Layered Li (NixMnyCoz)O2. *J. Am. Chem. Soc.* **2015**, *137*, 8364−8367.

(15) Yang, H.; Wu, H.-H.; Ge, M.; Li, L.; Yuan, Y.; Yao, Q.; Chen, J.; Xia, L.; Zheng, J.; Chen, Z.; Duan, J.; Kisslinger, K.; Zeng, X.-C.; Lee, W.-K.; Zhang, Q.; Lu, J. Simultaneously Dual Modification of Ni-Rich Layered Oxide Cathode for High-Energy Lithium-Ion Batteries. *Adv. Funct. Mater.* **2019**, *29*, 1808825.

(16) Yu, H.; Kim, H.; Wang, Y.; He, P.; Asakura, D.; Nakamura, Y.; Zhou, H. High-Energy "composite" Layered Manganese-Rich Cathode Materials via Controlling Li2MnO3 Phase Activation for Lithium-Ion Batteries. *Phys. Chem. Chem. Phys.* **2012**, *14*, 6584−6595.

(17) Jarvis, K. A.; Deng, Z.; Allard, L. F.; Manthiram, A.; Ferreira, P. J. Atomic Structure of a Lithium-Rich Layered Oxide Material for Lithium-Ion Batteries: Evidence of a Solid Solution. *Chem. Mater.* **2011**, *23*, 3614−3621.

(18) Yu, H.; Zhou, H. High-Energy Cathode Materials (Li2MnO3-LiMO2) for Lithium-Ion Batteries. *J. Phys. Chem. Lett.* **2013**, *4*, 1268−1280.

(19) Kim, G. S.; Johnson, C. S.; Thackeray, M. M. Layered XLiMO2·(1-x)Li2M′O3 Electrodes for Lithium Batteries: A Study of 0.95LiMn0.5Ni0.5O2·0.05Li2TiO3. *Electrochem. Commun.* **2002**, *4*, 205−209.

(20) Kim, J. S.; Johnson, C. S.; Vaughey, J. T.; Thackeray, M. M.; Hackney, S. A.; Yoon, W.; Grey, C. P. Electrochemical and Structural Properties of XLi2M′O3·(1-x)LiMn0.5Ni0.5O2 Electrodes for Lithium Batteries (M′ = Ti, Mn, Zr; O ≤x ≤ 0.3). *Chem. Mater.* **2004**, *16*, 1996−2006.

(21) Thackeray, M. M.; Kang, S. H.; Johnson, C. S.; Vaughey, J. T.; Hackney, S. A. Comments on the Structural Complexity of Lithium-Rich Li1+xM1-XO2 Electrodes (M = Mn, Ni, Co) for Lithium Batteries. *Electrochem. Commun.* **2006**, *8*, 1531−1538.

(22) Thackeray, M. M.; Kang, S. H.; Johnson, C. S.; Vaughey, J. T.; Benedek, R.; Hackney, S. A. Li2MnO3-Stabilized LiMO2 (M = Mn, Ni, Co) Electrodes for Lithium-Ion Batteries. *J. Mater. Chem.* **2007**, *17*, 3112−3125.

(23) Amalraj, F.; Kovacheva, D.; Talianker, M.; Zeiri, L.; Grinblat, J.; Leifer, N.; Goobes, G.; Markovsky, B.; Aurbach, D. Integrated Materials XLi2MnO3·(1 − x) LiMn1 / 3Ni1/3Co1/3O2 (x = 0.3, 0.5, 0.7) synthesized. *J. Electrochem. Soc.* **2010**, *157*, A1121−A1130.

(24) Johnson, C. S.; Li, N.; Lefief, C.; Vaughey, J. T.; Thackeray, M. M. Synthesis, Characterization and Electrochemistry of Lithium

Battery Electrodes: XLi2MnO3 · (1- x)LiMn0.333Ni0.333Co0.333O2 (0 ≤ x ≤ 0.7). *Chem. Mater.* **2008**, *20*, 6095−6106.
(25) Yu, C.; Li, G.; Guan, X.; Zheng, J.; Li, L.; Chen, T. Composites Li2MnO3·LiMn1/3Ni1/3Co1/3O2: Optimized Synthesis and Applications as Advanced High-Voltage Cathode for Batteries Working at Elevated Temperatures. *Electrochim. Acta* **2012**, *81*, 283−291.
(26) Liu, J.; Wang, Q.; Reeja-Jayan, B.; Manthiram, A. Carbon-Coated High Capacity Layered Li[Li0.2Mn0.54Ni0.13Co0.13]O2 Cathodes. *Electrochem. Commun.* **2010**, *12*, 750−753.
(27) Yu, H.; Zhou, H. Initial Coulombic Efficiency Improvement of the Li1.2Mn0.567Ni0.166Co0.067O2 Lithium-Rich Material by Ruthenium Substitution for Manganese. *J. Mater. Chem.* **2012**, *22*, 15507−15510.
(28) Gu, M.; Belharouak, I.; Zheng, J.; Wu, H.; Xiao, J.; Genc, A.; Amine, K.; Thevuthasan, S.; Baer, D. R.; Zhang, J.-G.; Browning, N. D.; Liu, J.; Wang, C. Formation of the Spinel Phase in the Layered Composite Cathode Used in Li-Ion Batteries. *ACS Nano* **2012**, *7*, 760−767.
(29) Mohanty, D.; Kalnaus, S.; Meisner, R. A.; Rhodes, K. J.; Li, J.; Payzant, E. A.; Wood, D. L., III; Daniel, C. Structural Transformation of a Lithium-Rich Li1.2Co 0.1Mn0.55Ni0.15O2 Cathode during High Voltage Cycling Resolved by in Situ X-Ray Diffraction. *J. Power Sources* **2013**, *229*, 239−248.
(30) Nayak, P. K.; Erickson, E. M.; Schipper, F.; Penki, T. R.; Munichandraiah, N.; Adelhelm, P.; Sclar, H.; Amalraj, F.; Markovsky, B.; Aurbach, D. Review on Challenges and Recent Advances in the Electrochemical Performance of High Capacity Li- and Mn-Rich Cathode Materials for Li-Ion Batteries. *Adv. Energy Mater.* **2018**, *8*, 1702397.
(31) Nayak, P. K.; Grinblat, J.; Levi, M.; Aurbach, D. Electrochemical and Structural Characterization of Carbon Coated Li 1.2Mn0.56Ni0.16Co0.08O2 and Li1.2Mn0.6Ni0.2O2 as Cathode Materials for Li-Ion Batteries. *Electrochim. Acta* **2014**, *137*, 546−556.
(32) Thackeray, M. M.; Johnson, C. S.; Vaughey, J. T.; Li, N.; Hackney, S. A. Advances in Manganese-Oxide "composite" Electrodes for Lithium-Ion Batteries. *J. Mater. Chem.* **2005**, *15*, 2257−2267.
(33) Li, Z.; Du, F.; Bie, X.; Zhang, D.; Cai, Y.; Cui, X.; Wang, C.; Chen, G.; Wei, Y. Electrochemical Kinetics of the Li[Li0.23Co0.3Mn 0.47]O2 Cathode Material Studied by GITT and EIS. *J. Phys. Chem. C* **2010**, *114*, 22751−22757.
(34) Park, M.; Zhang, X.; Chung, M.; Less, G. B.; Sastry, A. M. A Review of Conduction Phenomena in Li-Ion Batteries. *J. Power Sources* **2010**, *195*, 7904−7929.
(35) Hy, S.; Felix, F.; Rick, J.; Su, W. N.; Hwang, B. J. Direct in Situ Observation of Li2O Evolution on Li-Rich High-Capacity Cathode Material, Li[Nix Li(1-2x)/3Mn (2-x)/3]O2(0 ≤ x ≤0.5). *J. Am. Chem. Soc.* **2014**, *136*, 999−1007.
(36) Zhao, J.; Huang, R.; Gao, W.; Zuo, J.-M.; Zhang, X. F.; Misture, S. T.; Chen, Y.; Lockard, J. V.; Zhang, B.; Guo, S.; Khoshi, M. R.; Dooley, K.; He, H.; Wang, Y. An Ion-Exchange Promoted Phase Transition in a Li-Excess Layered Cathode Material for High-Performance Lithium Ion Batteries. *Adv. Energy Mater.* **2015**, *5*, 1−12.
(37) Deng, Y. P.; Yin, Z. W.; Wu, Z. G.; Zhang, S. J.; Fu, F.; Zhang, T.; Li, J. T.; Huang, L.; Sun, S. G. Layered/Spinel Heterostructured and Hierarchical Micro/Nanostructured Li-Rich Cathode Materials with Enhanced Electrochemical Properties for Li-Ion Batteries. *ACS Appl. Mater. Interfaces* **2017**, *9*, 21065−21070.
(38) Yu, R.; Zhang, X.; Liu, T.; Yang, L.; Liu, L.; Wang, Y.; Wang, X.; Shu, H.; Yang, X. Spinel/Layered Heterostructured Lithium-Rich Oxide Nanowires as Cathode Material for High-Energy Lithium-Ion Batteries. *ACS Appl. Mater. Interfaces* **2017**, *9*, 41210−41223.
(39) Bian, X.; Fu, Q.; Qiu, H.; Du, F.; Gao, Y.; Zhang, L.; Zou, B.; Chen, G.; Wei, Y. High-Performance Li-(Li0.18Ni0.15Co0.15Mn0.52)O2@Li4M5O12 Heterostructured Cathode Material Coated with a Lithium Borate Oxide Glass Layer. *Chem. Mater.* **2015**, *27*, 5745−5754.
(40) Zhang, J.; Gao, R.; Sun, L.; Li, Z.; Zhang, H.; Hu, Z.; Liu, X. Understanding the Effect of an: In Situ Generated and Integrated Spinel Phase on a Layered Li-Rich Cathode Material Using a Non-Stoichiometric Strategy. *Phys. Chem. Chem. Phys.* **2016**, *18*, 25711−25720.
(41) Thackeray, M. M.; de Kock, A.; Rossouw, M. H.; Liles, D.; Bittihn, R.; Hoge, D. Spinel Electrodes from the Li-Mn-O System for Rechargeable Lithium Battery Applications. *J. Electrochem. Soc.* **1992**, *139*, 363−366.
(42) Kitchaev, D. A.; Lun, Z.; Richards, W. D.; Ji, H.; Clément, R. J.; Balasubramanian, M.; Kwon, D. H.; Dai, K.; Papp, J. K.; Lei, T.; McCloskey, B. D.; Yang, W.; Lee, J.; Ceder, G. Design Principles for High Transition Metal Capacity in Disordered Rocksalt Li-Ion Cathodes. *Energy Environ. Sci.* **2018**, *11*, 2159−2171.
(43) Li, L.; Song, B. H.; Chang, Y. L.; Xia, H.; Yang, J. R.; Lee, K. S.; Lu, L. Retarded Phase Transition by Fluorine Doping in Li-Rich Layered Li 1.2 Mn 0.54 Ni 0.13 Co 0.13 O2 Cathode Material. *J. Power Sources* **2015**, *283*, 162−170.
(44) Kang, S.-H.; Amine, K. Layered Li(Li0.2Ni0.15 + 0.5zCo0.10Mn0.55 - 0.5z)O2 - ZFz Cathode Materials for Li-Ion Secondary Batteries. *J. Power Sources* **2005**, *146*, 654−657.
(45) Wang, Z. Q.; Chen, Y. C.; Ouyang, C. Y. Polaron States and Migration in F-Doped Li2MnO3. *Phys. Lett. A* **2014**, *378*, 2449−2452.
(46) Nandi, D. K.; Sen, U. K.; Dhara, A.; Mitra, S.; Sarkar, S. K. Intercalation Based Tungsten Disulfide (WS2) Li-Ion Battery Anode Grown by Atomic Layer Deposition. *RSC Adv.* **2016**, *6*, 38024−38032.
(47) Hawkins, C. G.; Whittaker-Brooks, L. Controlling Sulfur Vacancies in TiS2−x Cathode Insertion Hosts via the Conversion of TiS3 Nanobelts for Energy-Storage Applications. *ACS Appl. Nano Mater.* **2018**, *1*, 851−859.
(48) Stephenson, T.; Li, Z.; Olsen, B.; Mitlin, D. Lithium Ion Battery Applications of Molybdenum Disulfide (MoS2) Nanocomposites. *Energy Environ. Sci.* **2014**, *7*, 209−231.
(49) Zhao, L.; Wu, H.-H.; Yang, C.; Zhang, Q.; Zhong, G.; Zheng, Z.; Chen, H.; Wang, J.; He, K.; Wang, B.; Zhu, T.; Zeng, X.-C.; Liu, M.; Wang, M.-S. Mechanistic Origin of the High Performance of Yolk@Shell Bi2S3@N-Doped Carbon Nanowire Electrodes. *ACS Nano* **2018**, *12*, 12597−12611.
(50) Park, K. S.; Cho, M. H.; Jin, S. J.; Song, C. H.; Nahm, K. S. The Effects of Sulfur Doping on the Performance of O3-Li0.7 [Li1/12Ni1/12Mn5/6]O2 Powder. *Korean J. Chem. Eng.* **2005**, *22*, 560−565.
(51) An, J.; Shi, L.; Chen, G.; Li, M.; Liu, H.; Yuan, S.; Chen, S.; Zhang, D. Insights into the Stable Layered Structure of a Li-Rich Cathode Material for Lithium-Ion Batteries. *J. Mater. Chem. A* **2017**, *5*, 19738−19744.
(52) Zheng, J.; Myeong, S.; Cho, W.; Yan, P.; Xiao, J.; Wang, C.; Cho, J.; Zhang, J. G. Li- and Mn-Rich Cathode Materials: Challenges to Commercialization. *Adv. Energy Mater.* **2016**, *7*, 1601284.
(53) Carabineiro, S. A. C.; Bastos, S. S. T.; Órfão, J. J. M.; Pereira, M. F. R.; Delgado, J. J.; Figueiredo, J. L. Carbon Monoxide Oxidation Catalysed by Exotemplated Manganese Oxides. *Catal. Lett.* **2010**, *134*, 217−227.
(54) Verde, M. G.; Liu, H.; Carroll, K. J.; Baggetto, L.; Veith, G. M.; Meng, Y. S. Effect of Morphology and Manganese Valence on the Voltage Fade and Capacity Retention of Li[Li2/12Ni3/12Mn7/12]O2. *ACS Appl. Mater. Interfaces* **2014**, *6*, 18868−18877.
(55) Kresse, G.; Furthmüller, J. Efficient Iterative Schemes for Ab Initio Total-Energy Calculations Using a Plane-Wave Basis Set. *Phys. Rev. B* **1996**, *54*, 11169−11186.
(56) Perdew, J. P.; Burke, K.; Ernzerhof, M. Generalized Gradient Approximation Made Simple. *Phys. Rev. Lett.* **1996**, *77*, 3865−3868.
(57) Dudarev, S. L.; Botton, G. A.; Savrasov, S. Y.; Humphreys, C. J.; Sutton, A. P. Electron-Energy-Loss Spectra and the Structural Stability of Nickel Oxide: An LSDA+U Study. *Phys. Rev. B* **1998**, *57*, 1505−1509.
(58) Zhou, F.; Cococcioni, M.; Marianetti, C. A.; Morgan, D.; Ceder, G. First-Principles Prediction of Redox Potentials in Transition-Metal Compounds with LDA + U. *Phys. Rev. B* **2004**, *70*, 235121.

https://dx.doi.org/10.1021/acssuschemeng.0c02687
ACS Sustainable Chem. Eng. 2020, 8, 8037−8048

(59) Singh, D. J. Magnetic and Electronic Properties of LiMnO2s. *Phys. Rev. B* **1997**, *55*, 309−312.
(60) Kong, F.; Liang, C.; Longo, R. C.; Yeon, D. H.; Zheng, Y.; Park, J. H.; Doo, S. G.; Cho, K. Conflicting Roles of Anion Doping on the Electrochemical Performance of Li-Ion Battery Cathode Materials. *Chem. Mater.* **2016**, *28*, 6942−6952.
(61) Zhao, J.; Huang, R.; Gao, W.; Zuo, J.-M.; Zhang, X. F.; Misture, S. T.; Chen, Y.; Lockard, J. V.; Zhang, B.; Guo, S.; Khoshi, M. R.; Dooley, K.; He, H.; Wang, Y. An Ion-Exchange Promoted Phase Transition in a Li-Excess Layered Cathode Material for High-Performance Lithium Ion Batteries. *Adv. Energy Mater.* **2015**, *5*, 1401937.
(62) Girish, M.; Dhandayuthapani, T.; Sivakumar, R.; Sanjeeviraja, C.; Kumaresavanji, M. Substrate Temperature and Molar Ratio Induced Changes on the Properties of Nebulized Spray Deposited MnS Films. *J. Mater. Sci.: Mater. Electron.* **2017**, *28*, 6741−6753.
(63) Ragupathi, V.; Panigrahi, P.; Ganapathi Subramaniam, N. G-C3N4 Doped MnS as High Performance Electrode Material for Supercapacitor Application. *Mater. Lett.* **2019**, *246*, 88−91.
(64) Chen, Z.; Dahn, J. R. Methods to Obtain Excellent Capacity Retention in $LiCoO_2$ Cycled to 4.5 V. *Electrochim. Acta* **2004**, *49*, 1079−1090.
(65) Jiang, Q.; Liu, D.; Zhang, H.; Wang, S. Plasma-Assisted Sulfur Doping of LiMn2O4 for High-Performance Lithium-Ion Batteries. *J. Phys. Chem. C* **2015**, *119*, 28776−28782.
(66) Ramachandran, R.; Saranya, M.; Grace, A. N.; Wang, F. MnS Nanocomposites Based on Doped Graphene: Simple Synthesis by a Wet Chemical Route and Improved Electrochemical Properties as an Electrode Material for Supercapacitors. *RSC Adv.* **2017**, *7*, 2249−2257.
(67) Bian, X.; Fu, Q.; Pang, Q.; Gao, Y.; Wei, Y.; Zou, B.; Du, F.; Chen, G. Multi-Functional Surface Engineering for Li-Excess Layered Cathode Material Targeting Excellent Electrochemical and Thermal Safety Properties. *ACS Appl. Mater. Interfaces* **2016**, *8*, 3308−3318.
(68) Yan, P.; Nie, A.; Zheng, J.; Zhou, Y.; Lu, D.; Zhang, X.; Xu, R.; Belharouak, I.; Zu, X.; Xiao, J.; Amine, K.; Liu, J.; Gao, F.; Shahbazian-Yassar, R.; Zhang, J.-G.; Wang, C.-M. Evolution of Lattice Structure and Chemical Composition of the Surface Reconstruction Layer in Li1.2Ni0.2Mn0.6O2 Cathode Material for Lithium Ion Batteries. *Nano Lett.* **2014**, *15*, 514−522.
(69) Chen, M.; Xiang, X.; Chen, D.; Liao, Y.; Huang, Q.; Li, W. Polyethylene Glycol-Assisted Synthesis of Hierarchically Porous Layered Lithium-Rich Oxide as Cathode of Lithium Ion Battery. *J. Power Sources* **2015**, *279*, 197−204.
(70) Shen, S.; Hong, Y.; Zhu, F.; Cao, Z.; Li, Y.; Ke, F.; Fan, J.; Zhou, L.; Wu, L.; Dai, P.; Caim, M.; Huang, L.; Zhou, Z.; Li, J.; Wu, Q.; Sun, S. Tuning Electrochemical Properties of Li-Rich Layered Oxide Cathodes by Adjusting Co/Ni Ratios and Mechanism Investigation Using in Situ X-Ray Diffraction and Online Continuous Flow Differential Electrochemical Mass Spectrometry. *ACS Appl. Mater. Interfaces* **2017**, *10*, 12666−12677.
(71) Xu, G.; Liu, Z.; Zhang, C.; Cui, G.; Chen, L. Strategies for Improving the Cyclability and Thermo-Stability of LiMn2O4-Based Batteries at Elevated Temperatures. *J. Mater. Chem. A* **2015**, *3*, 4092−4123.
(72) Sun, W.; Cao, F.; Liu, Y.; Zhao, X.; Liu, X.; Yuan, J. Nanoporous LiMn2O4 Nanosheets with Exposed {111} Facets as Cathodes for Highly Reversible Lithium-Ion Batteries. *J. Mater. Chem.* **2012**, *22*, 20952−20957.
(73) Wang, D.; Wang, X.; Yu, R.; Bai, Y.; Wang, G.; Liu, M.; Yang, X. The Control and Performance of Li4Mn5O12 and Li2MnO3 Phase Ratios in the Lithium-Rich Cathode Materials. *Electrochim. Acta* **2016**, *190*, 1142−1149.
(74) Ramana, C. V.; Massot, M.; Julien, C. M. XPS and Raman Spectroscopic Characterization of LiMn2O 4 Spinels. *Surf. Interface Anal.* **2005**, *37*, 412−416.
(75) Yu, D. Y. W.; Yanagida, K. Structural Analysis of Li2MnO3 and Related Li-Mn-O Materials. *J. Electrochem. Soc.* **2011**, *158*, A1015−A1022.
(76) Biesinger, M. C.; Payne, B. P.; Grosvenor, A. P.; Lau, L. W. M.; Gerson, A. R.; Smart, R. S. C. Resolving Surface Chemical States in XPS Analysis of First Row Transition Metals, Oxides and Hydroxides: Cr, Mn, Fe, Co and Ni. *Appl. Surf. Sci.* **2011**, *257*, 2717−2730.
(77) Cho, Y.; Lee, S.; Lee, Y.; Hong, T.; Cho, J. Spinel-Layered Core-Shell Cathode Materials for Li-Ion Batteries. *Adv. Energy Mater.* **2011**, *1*, 821−828.
(78) Luo, D.; Li, G.; Fu, C.; Zheng, J.; Fan, J.; Li, Q.; Li, L. A New Spinel-Layered Li-Rich Microsphere as a High-Rate Cathode Material for Li-Ion Batteries. *Adv. Energy Mater.* **2014**, *4*, 1400062.
(79) Zhang, Y. C.; Wang, H.; Wang, B.; Yan, H.; Ahniyaz, A.; Yoshimura, M. Low Temperature Synthesis of Nanocrystalline Li4Mn5O12 by a Hydrothermal Method. *Mater. Res. Bull.* **2002**, *37*, 1411−1417.
(80) Takada, T.; Hayakawa, H.; Akiba, E.; Izumi, F.; Chakoumakos, B. C. Novel Synthesis Process and Structure Refinements of Li4Mn5O12 for Rechargeable Lithium Batteries. *J. Power Sources* **1997**, *68*, 613−617.
(81) Kataoka, R.; Taguchi, N.; Kojima, T.; Takeichi, N.; Kiyobayashi, T. Improving the Oxygen Redox Stability of NaCl-Type Cation Disordered Li2MnO3 in a Composite Structure of Li2MnO3 and Spinel-Type LiMn2O4. *J. Mater. Chem. A* **2019**, *7*, 5381−5390.
(82) Zhang, X. D.; Shi, J. L.; Liang, J. Y.; Yin, Y. X.; Zhang, J. N.; Yu, X. Q.; Guo, Y. G. Suppressing Surface Lattice Oxygen Release of Li-Rich Cathode Materials via Heterostructured Spinel Li4Mn5O12 Coating. *Adv. Mater.* **2018**, *30*, 1−8.
(83) Ivanova, S.; Zhecheva, E.; Nihtianova, D.; Stoyanova, R. Nano-Domain Structure of Li4Mn5O12 Spinel. *J. Mater. Sci.* **2011**, *46*, 7098−7105.
(84) Tian, Y.; Chen, D.; Jiao, X.; Duan, Y. Facile Preparation and Electrochemical Properties of Cubic-Phase Li4Mn5O12 Nanowires. *Chem. Commun.* **2007**, *20*, 2072−2074.

https://dx.doi.org/10.1021/acssuschemeng.0c02687
ACS Sustainable Chem. Eng. 2020, 8, 8037−8048